MATERIALS SCIENCE

Superconductivity in an ultrathin multilayer nickelate

Xi Yan[1], Hong Zheng[1], Yan Li[1], Hui Cao[1], Daniel Patrick Phelan[1], Hao Zheng[1], Zhan Zhang[2], Hawoong Hong[2], Guanyi Wang[3], Yuzi Liu[3], Anand Bhattacharya[1], Hua Zhou[2]*, Dillon D. Fong[1]*

We report the appearance of superconductivity in single-unit-cell $Nd_6Ni_5O_{12}$, exhibiting a transition temperature similar to that of thicker films. In situ synchrotron x-ray scattering performed during growth of the parent phase, $Nd_6Ni_5O_{16}$, shows that the necessary layer-by-layer deposition sequence does not follow the sequence of the formula unit but an alternate order due to the relative stability of the perovskite unit cell. We exploit this insight to grow ultrathin $Nd_6Ni_5O_{16}$ heterostructures and conduct in situ studies of topotactic reduction, finding that formation of the square-planar phase occurs rapidly and is highly sensitive to reduction temperature, with small deviations from the optimum condition leading to inhomogeneity and the loss of superconductivity. The fluorite layer within the unit cell facilitates reduction by initially stabilizing the square-planar phase in the upper half of the unit cell. Our findings provide insight into growth of the Ruddlesden-Popper nickelates, highlighting the need for in situ studies of the metastable phases key to superconductivity.

INTRODUCTION

Researchers have long sought analogs to the superconducting cuprates in other complex oxide systems. The nickelates were clear contenders, particularly if Ni could be stabilized in the 1+ state, thereby sharing the same $3d^9$ electronic configuration as Cu^{2+} in the cuprates (*1*, *2*). The recent discovery of superconductivity in the "infinite-layer" nickelate, $Nd_{0.8}Sr_{0.2}NiO_2$ (*3*), has led to considerable discussion as well as exploration of the structure in this and related systems (*4*–*10*). This has resulted in major debate on whether the intrinsic properties of the nickelates are directly analogous to those of other high-T_c superconductors (cuprates or even iron-based superconductors), and the increasing number of superconducting systems leads to important questions concerning the fundamental nature of high-T_c superconductivity (*7*, *11*–*13*). Furthermore, although superconductivity was observed in a $Nd_{0.8}Sr_{0.2}NiO_2$ thin film, it was found that T_c monotonically decreased with film thickness (*8*), completely suppressing it below 4.6 nm [e.g., 13 unit cells (UC)]. This led many to question whether this stems from extrinsic effects or whether T_c intrinsically depends on thickness and vanishes in the film dimensional limit.

Undoped $NdNiO_2$ represents the $n = \infty$ member of a family of layered square-planar nickelates with the chemical formula $R_{n+1}Ni_nO_{2n+2}$ where R denotes a rare earth cation (*14*). Rather than tuning the degree of electron filling through cation substitution, it is possible to alter the electronic behavior by varying the dimensionality, n. For instance, with $n = 5$ and $Nd_6Ni_5O_{12}$, as demonstrated by Pan *et al.* (*15*), the electronic configuration is $d^{8.8}$, placing it near the center of the superconducting dome (*15*–*17*). The three-dimensional (3D) structural disorder caused by chemical substitution can naturally be avoided in such structures (*18*), making $Nd_6Ni_5O_{12}$ an ideal candidate for studying the intrinsic properties of the superconducting nickelates. In addition, the 2D-like nature of $Nd_6Ni_5O_{12}$ allows inherent investigations into how film dimensionality mediates the superconducting transition.

Here, we demonstrate the appearance of superconductivity in single-unit-cell $Nd_6Ni_5O_{12}$ grown on $NdGaO_3$ by molecular beam epitaxy (MBE), exhibiting a thickness invariant superconducting transition as compared to thicker films. Conducting in situ synchrotron x-ray scattering during layer-by-layer growth by MBE, we find that growth of the $Nd_6Ni_5O_{12}$ precursor phase ($Nd_6Ni_5O_{16}$) cannot be attained by a layer sequence corresponding to the (001)-oriented crystal structure. Because of the occurrence of dynamic layer rearrangement, a phenomenon initially discovered for Sr_2TiO_4 and $La_3Ni_2O_7$ (*19*), we find that ultrathin $Nd_6Ni_5O_{16}$ must be grown by an alternate sequence accounting for interdiffusion during growth. Subsequent in situ studies of chemical reduction show that nucleation and growth of the superconducting $Nd_6Ni_5O_{12}$ phase occurs in a rapid mode and is extremely sensitive to reduction temperature, with nonideal conditions leading to defective regions and the loss of superconductivity.

RESULTS

Both the Sr-doped $NdNiO_2$ and the undoped $Nd_6Ni_5O_{12}$ films cannot be grown directly but must be converted from precursor films through topotactic reduction (*20*). For $Nd_6Ni_5O_{12}$, the as-grown film is $Nd_6Ni_5O_{16}$, the $n = 5$ member of the Ruddlesden-Popper (RP) family, $R_{n+1}Ni_nO_{3n+1}$. Reduction with CaH_2 (see Methods) results in the removal of the apical oxygen anions between two adjacent NiO_2 planes, with its electron filling changing from $d^{7.2}$ to $d^{8.8}$.

Achieving superconductivity in epitaxial $Nd_6Ni_5O_{12}$ films depends on an array of factors but most critically on the quality of $Nd_6Ni_5O_{16}$ (*21*–*23*). Growth of the RP nickelates with $n > 3$ is known to be highly challenging and can only be grown by a shuttered growth technique. To date, only a few independent groups have reported successful growth of the high-n RP oxides (*15*, *24*). We use a unique MBE system at the Advanced Photon Source, using synchrotron x-ray techniques to both monitor MBE growth (as a guide for atomically precise deposition) and characterize the film during any stage in situ (see Methods) (*25*). Unlike the more common in situ growth characterization tool, reflection high-energy electron diffraction (RHEED), synchrotron x-rays penetrate through the entirety of the film, and surface-sensitive probing allows layer-by-layer reconstruction of the atomic structure with sub-angstrom resolution. In situ x-ray characterization

[1]Materials Science Division, Argonne National Laboratory, Lemont, IL 60439, USA. [2]X-ray Science Division, Advanced Photon Source, Argonne National Laboratory, Lemont, IL 60439, USA. [3]Center for Nanoscale Materials, Argonne National Laboratory, Lemont, IL 60439, USA.
*Corresponding author. Email: hzhou@anl.gov (H.Z.); fong@anl.gov (D.D.F.)

allows us to attain high sample quality in terms of thin film crystallinity and lattice coherency during both MBE growth and chemical reduction processes.

Electrical transport measurements

As shown on the left in Fig. 1A, the formula unit of $Nd_6Ni_5O_{16}$ consists of five successive perovskite layers of $NdNiO_3$ capped by an another plane of NdO, which represents a half-complete structural UC. The next five-layer perovskite group is displaced by half a lattice constant along the in-plane direction such that 1 UC is composed of 10 perovskite layers with a Nd_2O_2 rock salt layer at the center. After topotactic reduction, the structure is converted to $Nd_6Ni_5O_{12}$ (the right in Fig. 1A) with every five NiO_2 planes with square-planar coordination separated by a NdO_2 fluorite slab: $(NdO_2)^-[(NdNiO_2)_5]^+$.

As shown in Fig. 1B, the temperature dependence of the resistivity was measured for a 3-UC-thick film before and after the reduction. (The x-ray specular Bragg rods for the 3-UC $Nd_6Ni_5O_{16}$ and $Nd_6Ni_5O_{12}$ phases are shown in fig. S1.) The $Nd_6Ni_5O_{16}$ film exhibits a typical metal-to-insulator transition (MIT) at ~135 K with little hysteresis, reminiscent of the first-order transition observed in $NdNiO_3$. After reduction, the 3-UC film becomes superconducting although without reaching zero-ohm state, as shown at the bottom in Fig. 1B. The onset of the superconductivity is at ~17 K with the point of maximum curvature at ~10 K, consistent with the results from ref. (*15*).

$Nd_6Ni_5O_{12}$ films with a thickness of only 1 UC (which consists of multiple nickel oxide square-planar layers within it) also show an abrupt drop in resistivity with the onset of transition at temperatures as high as that of the 3-UC films (fig. S2) and the ~6-UC films previously reported (*15*). This invariance of T_c on film thickness is unlike that observed for $Nd_{0.8}Sr_{0.2}NiO_2$ (*8*) and may have important physical implications for our understanding of superconductivity and its mechanism in the nickelates. (The very different normal state resistivities and 2D sheet resistances for the different thickness films are also interesting and the subject of current investigation.) Figure 1C shows the suppression of superconductivity by an out-of-plane magnetic field for the 1-UC-thick film. Similar to ref. (*15*), we find an in-plane zero-temperature Ginsburg-Landau coherence length of $\xi_{ab}(0) = 30.4 \pm 0.3$ Å, using the field strength where the resistivity reaches 90% of the normal state as a proxy for the upper critical field (Fig. 1D).

In situ X-ray studies of growth

In contrast to in situ RHEED, where the behavior of the intensity oscillation depends strongly on the incident angle of the electron beam (*26*), x-ray intensity oscillations at anti-Bragg positions (lying midway between the Bragg peaks) are at a maximum when the grown atomic layer is complete (*27*, *28*). We therefore monitor the intensity of the $00\frac{1}{2}$ r.l.u. (one of the anti-Bragg positions) to study MBE growth behavior in situ; along the in-plane directions, the film is epitaxially strained to the substrate. The unit of r.l.u. refers to reciprocal lattice units, as defined by the lattice parameter of $NdGaO_3$ at the growth temperature. Our deposition started with a single layer of NdO on pseudocubic (001) $NdGaO_3$ (NGO) substrates with mix-terminated surfaces as quantified by coherent Bragg rod analysis or COBRA (fig. S3). The intensity oscillations of the first 5 UC of $NdNiO_3$, ending with a NdO adlayer (i.e., five perovskite layers of $NdNiO_3$ + NdO) indicate the layer-by-layer growth mode (fig. S4), with the resulting specular Bragg rod shown in fig. S3E (the green curve) and the corresponding extracted atomic structure in fig. S3F. According to Fig. 1A, the subsequent layers should be NdO → NiO_2 → NdO to form the rock salt slab and an additional $NdNiO_3$ UC; the growth oscillations at the $00\frac{1}{2}$ r.l.u. are

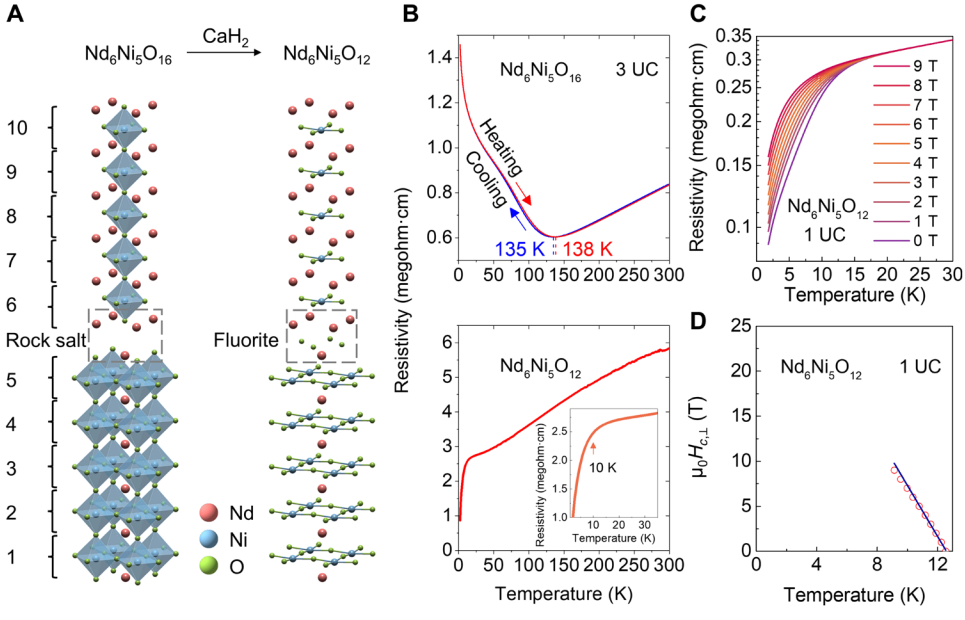

Fig. 1. Atomic structure and transport properties of 1- and 3-UC-thick $Nd_6Ni_5O_{16}$ and $Nd_6Ni_5O_{12}$ films. (**A**) UC structures of $Nd_6Ni_5O_{16}$ (left) and $Nd_6Ni_5O_{12}$ (right). (**B**) Resistivity versus temperature [$\rho(T)$] profiles measured while cooling and subsequent heating for the $Nd_6Ni_5O_{16}$ RP compound with 3 UC in thickness (top) and cooling after reduction to the $Nd_6Ni_5O_{12}$ phase (bottom). The point of maximum curvature of the transition is ~10 K, as shown in the inset. The resistivity was measured down to 1.8 K. (**C**) Field dependence of the $\rho(T)$ profile for the 1-UC-thick $Nd_6Ni_5O_{12}$ film. (**D**) Temperature dependence of the upper critical field $H_{c,\perp}$ with a linear scaling fit in the vicinity of T_c for the 1-UC-thick $Nd_6Ni_5O_{12}$ film.

presented in Fig. 2C. The deposition of NdO tends to form islands (roughening of the surface), thus leading to the intensity decrease, and the increase in the intensity is primarily due to smoothing of the surface by growing NiO_2. The specular Bragg rod was immediately measured after the growth of 1 UC of $Nd_6Ni_5O_{16}$, as shown in Fig. 2E. As illustrated by the blue curve, the 00*L* Bragg rod displays substantial structural complexity and nonperiodicity, particularly from $L = 0.5$ to $L = 2$ r.l.u., implying the presence of disorder or a misstacked structure. This can be compared with the calculated 00*L* Bragg rod for the ideal $Nd_6Ni_5O_{16}$ on GaO-terminated $NdGaO_3$, as shown in fig. S5. However, we find that if two successive layers of NdO are grown on NdO-terminated $NdNiO_3$, as demonstrated by the growth oscillations shown in Fig. 2D, the resulting specular Bragg rod shown in Fig. 2F is similar to the calculated 00*L* (fig. S5). A comparison between the structures resolved by COBRA and scanning transmission electron microscopy (STEM) deposited by the different growth sequences are illustrated in fig. S6.

We therefore find that, to avoid the dynamic rearrangement from NdO→NdO→NiO_2 to NdO→NiO_2→NdO in the high-temperature environment (here, the growth of the first NdO layer in this sequence indicates a completion of the 0.5-UC-thick $Nd_6Ni_5O_{16}$ film), an additional layer of NdO is required atop the rock salt slab (Fig. 2, A and B). In other words, three consecutive layers of NdO must be deposited prior to the perovskite layers: NdO → NdO → NdO → NiO_2 rather than NdO → NdO → NiO_2. This dynamic layer rearrangement was also observed during the growth of the Sr_2TiO_4 and $La_3Ni_2O_7$ RP phases (*19*, *29*) on $SrTiO_3$ (001) and adopted in growing the multilayer nickelate (*30*). The complex specular Bragg rod shown in Fig. 2E indicates the dynamic rearrangement is not complete and that the kinetics of rearrangement and the concurrent deposition may be comparable, resulting in a misstacked structure.

The specular Bragg rods for $Nd_6Ni_5O_{16}$ thin films with thicknesses varying from 1 UC to 3 UC at the growth temperature (560°C) are shown in Fig. 3A. All growths used the NdO → NdO → NdO → NiO_2 sequence. The even-numbered superlattice peaks are evident even just after the deposition of the thinnest 1-UC film. The peaks become sharper for the 2-UC film, and no peak splitting is observed, indicating single-phase $Nd_6Ni_5O_{16}$ with high crystalline

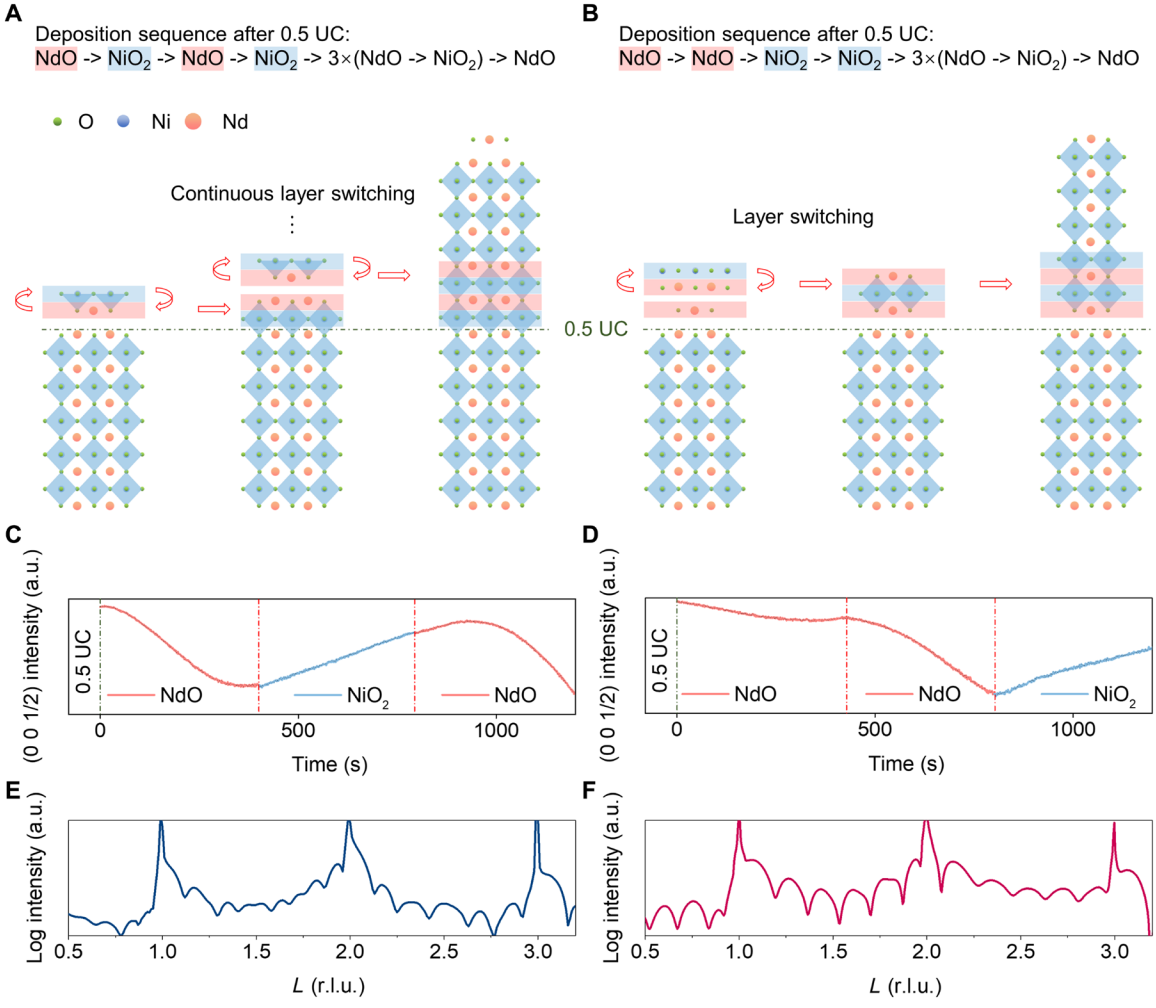

Fig. 2. Different growth sequences and in situ X-ray measurements. (**A** and **B**) The dynamic rearrangement occurs when depositing NdO→ NiO_2 on top of the 0.5-UC-thick $Nd_6Ni_5O_{16}$ film in the high-temperature environment. To avoid this, an additional layer of NdO is required atop the rock salt slab. Intensity at the $00\frac{1}{2}$ r.l.u. measured at 560°C during growth of the NdO→ NiO_2→ NdO sequence (**C**) versus the NdO→ NdO→ NiO_2 sequence (**D**). a.u., arbitrary units. The resulting specular Bragg rods after the growth of 1 UC using the [(C) and (D)] growth sequences are shown in (**E**) and (**F**), respectively.

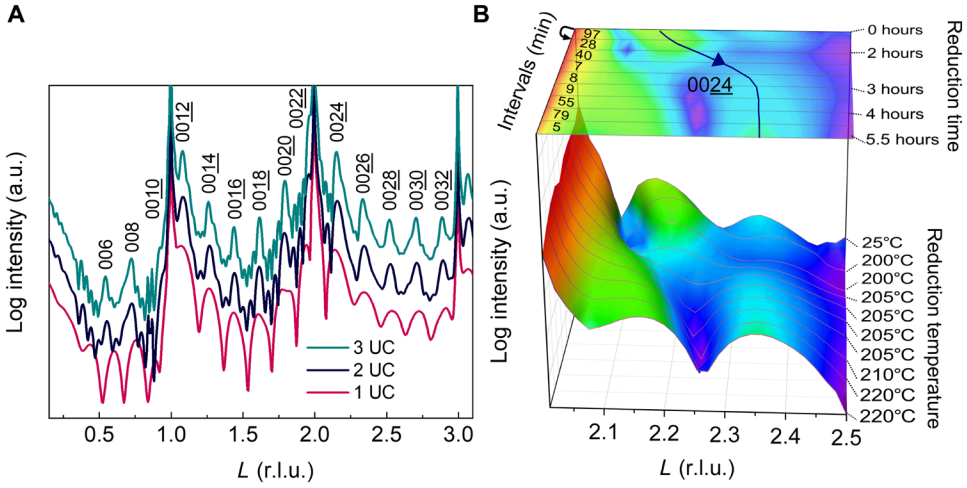

Fig. 3. In situ synchrotron X-ray results for the growth and topotactic reduction of $Nd_6Ni_5O_{16}$ thin films. (**A**) Measurements of the specular rod for 1-, 2-, and 3-UC-thick $Nd_6Ni_5O_{16}$ films grown on $NdGaO_3$ substrates. (**B**) Map of specular rods measured for the 1-UC-thick film at different temperatures in the CaH_2 reducing environment. The arrowed profile at the top shows the shift of the 00$\underline{24}$ reflection. The time intervals between each scan are calculated from the start time for each scan, and because the scans themselves require at least 7 to 8 min to process, the actual reduction time may be even shorter. The reduction time is nonlinear and represents the total time starting with the room temperature scan (0 hours).

quality (*31*). A 3-UC sample grown with the NdO → NdO → NiO_2 sequence was also made for comparison, with the specular Bragg rod shown in fig. S5B. As observed, the film is poorly ordered, exhibiting no RP-phase dedicated superlattice reflections.

In situ X-ray studies of reduction

We initially conducted ex situ CaH_2 reduction experiments to investigate the effects of the reduction time and temperature on phase formation. (Note that, because the heaters used for ex situ reduction and in situ reduction with x-ray monitoring are distinct, there may be an offset in temperature.) Here, in situ reduction and ex situ reduction refer to reduction experiments performed with and without x-ray monitoring, respectively. As shown in fig. S7, we find that the occurrence of superconductivity is highly sensitive to the topotactic reduction conditions and especially temperature. Differences as small as 5°C compared with the optimal temperature (260°C for the samples shown in fig. S7C) can result in an insulating (265°C) or semiconducting state (255°C) (with an MIT at 76 K), due to incomplete/inhomogeneous reduction. The specular Bragg rods for these 3-UC films are provided in fig. S7 (B and D). For the sample that later exhibited superconductivity, the specular Bragg rod shows the sharpest peaks and the smallest out-of-plane lattice constant (orange profile in fig. S7D), all of which suggests that any inhomogeneity within the $Nd_6Ni_5O_{16}$ precursor film can lead to substantial nonsuperconducting $Nd_6Ni_5O_{12\pm x}$ regions.

Given the sensitivity of the film properties to the reducing conditions, an in situ reduction experiment was designed to monitor the out-of-plane structure as $Nd_6Ni_5O_{16}$ transforms into the square-planar $Nd_6Ni_5O_{12}$ phase. Figure 3B shows the specular Bragg rod for the 1-UC film as it evolves with time and changes to the reduction temperature, focusing on the region near the 00$\underline{24}$ reflection. Both the intervals between scans at the same reduction temperature and the number of the scans at each temperature depended on the progress of scattering, i.e., 00*L* scans were collected until the intensity and position of the 00$\underline{24}$ reflection no longer changed, at which point the reduction temperature was increased. At 205°C, the 00$\underline{24}$ peak moved from 2.20 to 2.35 r.l.u. in the space of a few minutes, as indicated by the arrow on the projection of the peak intensities shown at the top of the figure. Note that the time intervals are calculated from the start time for each scan, and because the scans themselves require at least 7 to 8 min to process, the time for the actual reduction may be even shorter. Therefore, in contrast to the conventional understanding of a slow topotactic transition, our observation reveals that it primarily occurs in a rapid mode. This final state was confirmed to exhibit superconductivity as discussed above.

COBRA (*32*) was performed on scans with relatively large *L* range for the 1-UC film detailed in fig. S8. The out-of-plane lattice constant (equivalent to thickness for the 1-UC film) is 42.6 Å for $Nd_6Ni_5O_{16}$ and ~39.7 Å for $Nd_6Ni_5O_{12}$ (fig. S9). COBRA allows extraction of the precise positions of each atomic plane in the out-of-plane direction, and we summarize the lattice spacings for all the layers at the different reduction temperatures in Fig. 4A. Here, the vertical axis refers to the number of the perovskite layer from one NdO plane to the next NdO. The position of $Z = 0$ refers to the topmost NdO plane of the NGO substrate, which is the bottommost plane in Fig. 4B. As seen by the 200°C profile (pink diamonds), the overall layer spacing for each perovskite layer starts to decrease, indicating that some oxygen anions start to be extracted at this temperature (Fig. 4B). After the phase change at 205°C, the green diamond profile shows that the layer spacing contracts notably near the interface region (at the $Z = 2$ perovskite layer) and at the surface (at $Z = 7$ to 10 perovskite layers), whereas the lattice spacings near the fluorite slab ($Z = 3$ to 6 perovskite layers) do not exhibit notable changes. With higher reducing temperatures (210° to 220°C), more oxygen is lost, even in the fluorite slab, and the lattice spacings in the interface region, the central region, and the surface region ($Z = 8$ to 10 perovskite layers) stabilize near ~3.5 Å. The reduction process converts the rock salt NdO layers to the fluorite structure, and its layer spacing at different reduction temperatures is shown in fig. S10.

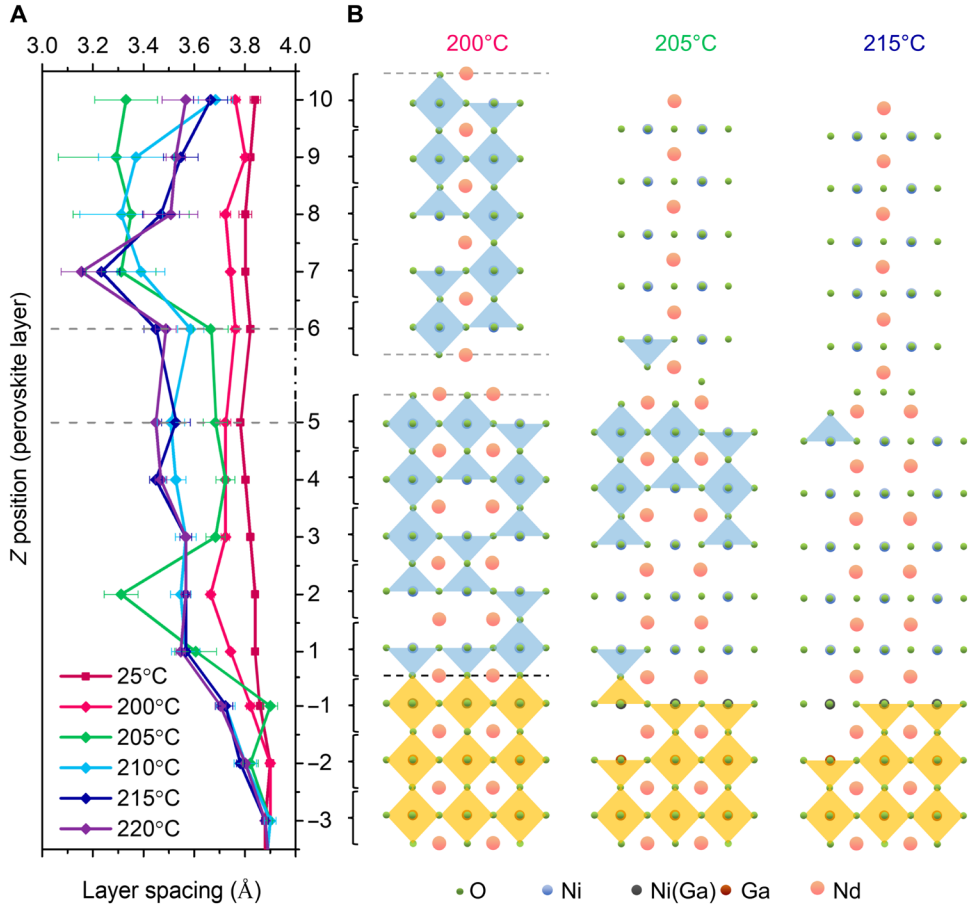

Fig. 4. Results on the out-of-plane atomic structure for the 1-UC-thick $Nd_6Ni_5O_x$ film during reduction as determined by COBRA. (**A**) Layer spacing profiles for the film at different temperatures. Here, the layer spacing refers to the distance from one NdO plane to the next NdO in the perovskite layer. The vertical axis refers to the number of the perovskite layer from one NdO plane to the next NdO. (**B**) Corresponding schematic illustrations of the out-of-plane structure at different temperatures during reduction.

The results suggest that the surface atomic layers of $Nd_6Ni_5O_{16}$ is the first part of the film to lose oxygen with Nd_2O_2 serving as a small barrier to loss, as may be expected based on the nature of the reduction process. The fluorite slab could assist to stabilize the square-planar phase under a high compressive strain and help to promote the topotactic reduction process (*33*). It is also worth noting that fine tuning of the reduction temperature could greatly promote the superconducting properties by expanding the superconducting dome with a higher onset of the superconducting transition temperature and a wider doping region (*34*).

DISCUSSION

As shown in Fig. 4A, we observed that before reaching the superconducting $Nd_6Ni_5O_{12}$ phase, the out-of-plane lattice constant does not contract uniformly in the intermediate state: There is a larger contraction in certain inner NiO_2 perovskite layers. This nontrivial behavior during reduction could be crucial for understanding the superconducting mechanism of nickelates and further promoting their performance. For the optimal Sr-doped infinite-layer nickelate superconductor, T_c would increase monotonically with applied physical pressure, which may result from enhanced electron hybridization between the 5d rare-earth layer and the 3d nickel layer due to the contraction of the out-of-plane lattice constant (*35*, *36*). In another aspect, Krieger *et al.* (*37*) suggested that an increase in the NiO_2 interplanar distance could reduce the role of the rare-earth electronic states on the NiO_2 planes, thereby extending the stability of the superconducting state in nickelates. In these regards, controlling the out-of-plane NiO_2 interplanar distance via fine-tuning reduction conditions and epitaxial strains could facilitate achieving the optimal point in balancing superconducting properties and phase stability.

The average valence state of Ni in the reduced films with an ideal structure is deduced to be 1.2+, but the actual Ni valence in our ultrathin film may qualitatively differ from that in the bulk form. The nonuniform out-of-plane NiO_2 interplanar distance could induce spatially inhomogeneous electronic states. Although the quintuple-layer nickelate film has three different symmetry-inequivalent Ni sites (Fig. 1A), it was theoretically predicted that the inner Ni site is favored by a d_{z^2} character with a slightly higher 3d count (*38*), which may support the Ni-d_{z^2}–driven flat-band physics for the stabilization of the superconducting phase. An experimental study on a high-T_c five-layer cuprate reported that Fermi pockets are observed only in the inner CuO_2 planes, where superconductivity is suggested to occur (*39*). Therefore, techniques such as electron energy-loss

spectroscopy are required to resolve the layer distribution of the electronic state of Ni.

We also noticed that the resistivity of the 1-UC sample in its intermediate state exhibits roughly logarithmic temperature dependence, as shown in fig. S11. Similar logarithmic behaviors at low temperatures were also seen in undoped $LaNiO_2$ films (*40*) and underdoped $R_{1-x}Sr_xNiO_2$ systems (*4*, *16*, *17*, *41*). The details regarding the origin of the observed transport behavior are discussed in the Supplementary Materials.

The broad superconducting transition profile may be affected by properties of the substrate-nickelate interface in the single-unit-cell limit, unlike the freestanding cuprate monolayer (*42*). Another notable example of superconductivity being affected by interfacial coupling with the substrate is MBE-grown monolayer FeSe/$SrTiO_3$ (*43*–*45*). Recently, a single atomic layer of Nd(Ti,Ni)O_3 was discovered by Goodge *et al.* (*46*) to form at the interface between the square-planar nickelate and the $SrTiO_3$ substrate. The existence of this layer is presumed to almost entirely quench the potential two-dimensional electron gas due to the polar discontinuity at the interface. Furthermore, some lattice strain may be needed to stabilize superconductivity in the thin-film geometry for both Sr-doped $NdNiO_2$ and $Nd_6Ni_5O_{12}$. The role of epitaxial strain on synthesis was studied for the $Nd_4Ni_3O_{10}$ system, and the authors found that the tensile strain (here grown on a $SrTiO_3$ substrate) tends to induce extended defects (*33*). As was shown in fig. S3, the mixed termination of the NGO substrates is likely to lead to an intermixed interface; therefore, the topotactic reaction is not confined to the nickelate film as lattice shrinkage appears from the nickelate-NGO interface down to two perovskite UC into the substrate (Fig. 4A). Nevertheless, we achieved superconductivity in the 1-UC limit with an onset temperature as high as that in thicker films, in sharp contrast to the decrease in T_c or the loss of superconductivity in the ultrathin infinite-layer films (*8*). The proposed thickness-driven multiband structure modification due to the enhanced Ni-O hybridization with reducing thickness (*8*) may be unimportant in the context of the RP multilayered superconducting nickelates. The quasi-2D quintuple-layer may provide a unique framework for electronic phase robustness, insusceptible to structural perturbations. Our results experimentally push nickelate superconductors to the 2D limit, thus offering an unprecedented platform for investigating quantum phenomena and innovative devices.

In summary, by using in situ synchrotron x-ray scattering during oxide MBE, we find that growth of ultrathin $Nd_6Ni_5O_{16}$ films does not follow the RP formula unit layer sequence but requires an additional NdO layer in between, due to the occurrence of layer rearrangement during MBE. Subsequent in situ studies of the topotactic reduction of the 1-UC-thick film show that the loss of oxygen occurs quickly at temperatures near 205°C, with little to no loss in crystal quality or interfacial roughness. We demonstrate that the resulting 1-UC and 3-UC $Nd_6Ni_5O_{12}$ films exhibit superconductivity with an onset temperature of ~17 K (and the point of maximum curvature ~10 K), as high as that of thicker films. The appearance of superconductivity is highly sensitive to the precise reduction conditions, with changes of even 5°C leading to insulating behavior. Cross-sectional structural snapshots of the 1-UC $Nd_6Ni_5O_x$ film during the reduction, performed with x-ray phase retrieval techniques, indicate that the reduction occurs in two stages, with the upper half of the $Nd_6Ni_5O_x$ UC forming square-planar layers prior to the bottom half, suggesting that the reduction of thicker films may result in a complete reduction only in layers closer to the surface.

The in situ x-ray results and structural details discussed here provide much needed information for quantitative calculations of the electronic structure as well as a method for the synthesis of other possible layered superconductors, e.g., those with other cations and/or higher-order RP sequences. Although superconductivity is difficult to achieve in bulk nickelates (*47*, *48*), compelling progress has been recently made with the application of pressure (*49*), indicating that strain is yet another variable of interest. We lastly note that the 2D-like properties of $Nd_6Ni_5O_{12}$ suggest a platform for the exploration of other emergent or coupled properties when layered with other functional materials, possibly with the aid of freestanding techniques (*50*).

METHODS

Oxide MBE with in situ SXRD

Thin film growth and in situ surface x-ray diffraction (SXRD) measurements were conducted at 33-ID-E of the Advanced Photon Source, using the oxide MBE chamber (*25*). The fluxes of the Nd and Ni sources were calibrated with a quartz crystal microbalance. The substrates were heated to 560°C at a rate of 15°C/min. After the temperature was stabilized at 560°C, as determined by an infrared optical pyrometer, NdO and NiO_2 were grown under an oxygen partial pressure of 2.0×10^{-6} mbar. The specular and diffuse intensities were simultaneously measured with a Pilatus 100K area detector.

In situ CaH_2 reduction

The as-grown nickelate films (~2.5 by 2.5 mm^2) were attached to a flat metal block and sealed within a quartz tube with 0.2 g of CaH_2 powder maintained at ~1 mtorr. The quartz tube was mounted on a six-circle x-ray diffractometer at sector 33-ID-D and heated for the in situ synchrotron x-ray experiment. The heating and cooling rates were fixed at 6°C/min.

Physical properties measurement

Transport measurements from 1.8 to 300 K were conducted with the four-probe method in the commercial Physical Property Measurement System allowing magnetic fields up to 9 T.

X-ray analysis

The x-ray scattering data were analyzed using the COBRA method (*32*). COBRA is a phase retrieval algorithm applicable to systems that are periodic in 2D and aperiodic in the out-of-plane direction, making it suitable for the analysis of SXRD data. The 3D electron density has sub-angstrom resolution. For the cases studied here, the known bulk structure of $NdNiO_3$ was used as a reference.

STEM characterization

The samples were prepared by a regular focused ion beam (FIB) lift-out process. A 100-nm-thick Au layer was deposited on sample surfaces before the samples were loaded to FIB to have the surfaces protected. At the final stage of FIB thinning, a 5-kV Ga ion beam was used to reduce material damage. The cross-sectional TEM samples were imaged by the Thermo Fisher Scientific Spectra 200 operated at 200 kV. The high-angle annular dark-field images were acquired in the angle range of 72 to 200 mrad.

Supplementary Materials

This PDF file includes:

Figs. S1 to S11
References

REFERENCES AND NOTES

1. M. R. Norman, Entering the nickel age of superconductivity. *Physics* **13**, 85 (2020).
2. W. E. Pickett, The dawn of the nickel age of superconductivity. *Nat. Rev. Phys.* **3**, 7–8 (2021).
3. D. Li, K. Lee, B. Y. Wang, M. Osada, S. Crossley, H. R. Lee, Y. Cui, Y. Hikita, H. Y. Hwang, Superconductivity in an infinite-layer nickelate. *Nature* **572**, 624–627 (2019).
4. M. Osada, B. Y. Wang, B. H. Goodge, S. P. Harvey, K. Lee, D. Li, L. F. Kourkoutis, H. Y. Hwang, Nickelate superconductivity without rare-earth magnetism: (La,Sr)NiO_2. *Adv. Mater.* **33**, e2104083 (2021).
5. B. Y. Wang, D. Li, B. H. Goodge, K. Lee, M. Osada, S. P. Harvey, L. F. Kourkoutis, M. R. Beasley, H. Y. Hwang, Isotropic Pauli-limited superconductivity in the infinite-layer nickelate $Nd_{0.775}Sr_{0.225}NiO_2$. *Nat. Phys.* **17**, 473–477 (2021).
6. Z. Chen, M. Osada, D. Li, E. M. Been, S.-D. Chen, M. Hashimoto, D. Lu, S.-K. Mo, K. Lee, B. Y. Wang, F. Rodolakis, J. L. McChesney, C. Jia, B. Moritz, T. P. Devereaux, H. Y. Hwang, Z.-X. Shen, Electronic structure of superconducting nickelates probed by resonant photoemission spectroscopy. *Matter* **5**, 1806–1815 (2022).
7. J. Fowlie, M. Hadjimichael, M. M. Martins, D. Li, M. Osada, B. Y. Wang, K. Lee, Y. Lee, Z. Salman, T. Prokscha, J.-M. Triscone, H. Y. Hwang, A. Suter, Intrinsic magnetism in superconducting infinite-layer nickelates. *Nat. Phys.* **18**, 1043–1047 (2022).
8. S. W. Zeng, X. M. Yin, C. J. Li, L. E. Chow, C. S. Tang, K. Han, Z. Huang, Y. Cao, D. Y. Wan, Z. T. Zhang, Z. S. Lim, C. Z. Diao, P. Yang, A. T. S. Wee, S. J. Pennycook, A. Ariando, Observation of perfect diamagnetism and interfacial effect on the electronic structures in infinite layer $Nd_{0.8}Sr_{0.2}NiO_2$ superconductors. *Nat. Commun.* **13**, 743 (2022).
9. X. Ding, C. C. Tam, X. Sui, Y. Zhao, M. Xu, J. Choi, H. Leng, J. Zhang, M. Wu, H. Xiao, X. Zu, M. Garcia-Fernandez, S. Agrestini, X. Wu, Q. Wang, P. Gao, S. Li, B. Huang, K.-J. Zhou, L. Qiao, Critical role of hydrogen for superconductivity in nickelates. *Nature* **615**, 50–55 (2023).
10. W. Wei, D. Vu, Z. Zhang, F. J. Walker, C. H. Ahn, Superconducting $Nd_{1-x}Eu_xNiO_2$ thin films using in situ synthesis. *Sci. Adv.* **9**, eadh3327 (2023).
11. T. Xie, Z. Liu, C. Cao, Z. Wang, J. Yang, W. Zhu, Microscopic theory of superconducting phase diagram in infinite-layer nickelates. *Phys. Rev. B* **106**, 035111 (2022).
12. C.-J. Kang, G. Kotliar, Optical properties of the infinite-layer $La_{1-x}Sr_xNiO_2$ and hidden Hund's physics. *Phys. Rev. Lett.* **126**, 127401 (2021).
13. J. F. Mitchell, A nickelate renaissance. *Front. Phys.* **9**, 813483 (2021).
14. P. Lacorre, Passage from T-type to T′-type arrangement by reducing $R_4Ni_3O_{10}$ to $R_4Ni_3O_8$ (R = La, Pr, Nd). *J. Solid State Chem.* **97**, 495–500 (1992).
15. G. A. Pan, D. Ferenc Segedin, H. LaBollita, Q. Song, E. M. Nica, B. H. Goodge, A. T. Pierce, S. Doyle, S. Novakov, D. Córdova Carrizales, A. T. N'Diaye, P. Shafer, H. Paik, J. T. Heron, J. A. Mason, A. Yacoby, L. F. Kourkoutis, O. Erten, C. M. Brooks, A. S. Botana, J. A. Mundy, Superconductivity in a quintuple-layer square-planar nickelate. *Nat. Mater.* **21**, 160–164 (2022).
16. D. Li, B. Y. Wang, K. Lee, S. P. Harvey, M. Osada, B. H. Goodge, L. F. Kourkoutis, H. Y. Hwang, Superconducting dome in $Nd_{1-x}Sr_xNiO_2$ infinite layer films. *Phys. Rev. Lett.* **125**, 027001 (2020).
17. S. Zeng, C. S. Tang, X. Yin, C. Li, M. Li, Z. Huang, J. Hu, W. Liu, G. J. Omar, H. Jani, Z. S. Lim, K. Han, D. Wan, P. Yang, S. J. Pennycook, A. T. S. Wee, A. Ariando, Phase diagram and superconducting dome of infinite-layer $Nd_{1-x}Sr_xNiO_2$ thin films. *Phys. Rev. Lett.* **125**, 147003 (2020).
18. M. Gabay, S. Gariglio, J.-M. Triscone, Functionally doped infinite-layer nickelates. *Nat. Mater.* **21**, 139–140 (2022).
19. J. Lee, G. Luo, I.-C. Tung, S. Chang, Z. Luo, M. Malshe, M. Gadre, A. Bhattacharya, S. Nakhmanson, J. Eastman, H. Hong, J. Jellinek, D. Morgan, D. D. Fong, J. W. Freeland, Dynamic layer rearrangement during growth of layered oxide films by molecular beam epitaxy. *Nat. Mater.* **13**, 879–883 (2014).
20. M. Crespin, P. Levitz, L. Gatineau, Reduced forms of $LaNiO_3$ perovskite. Part 1.—Evidence for new phases: $La_2Ni_2O_5$ and $LaNiO_2$. *J. Chem. Soc. Faraday Trans. 2* **79**, 1181–1194 (1983).
21. K. Lee, B. H. Goodge, D. Li, M. Osada, B. Y. Wang, Y. Cui, L. F. Kourkoutis, H. Y. Hwang, Aspects of the synthesis of thin film superconducting infinite-layer nickelates. *APL Mater.* **8**, 041107 (2020).
22. G. A. Pan, Q. Song, D. F. Segedin, M.-C. Jung, H. El-Sherif, E. E. Fleck, B. H. Goodge, S. Doyle, D. C. Carrizales, P. Shafer, H. Paik, L. F. Kourkoutis, I. E. Baggari, A. S. Botana, C. M. Brooks, J. A. Mundy, Synthesis and electronic properties of $Nd_{n+1}Ni_nO_{3n+1}$ Ruddlesden-Popper nickelate thin films. *Phys. Rev. Mater.* **6**, 055003 (2022).
23. Y. Ji, X. Gao, J. Liu, L. Li, K. Chen, Z. Liao, Stoichiometry, orbital configuration, and metal-to-insulator transition in $Nd_{0.8}Sr_{0.2}NiO_3$ films. *ACS Appl. Mater. Interfaces* **15**, 11353–11359 (2023).
24. Z. Li, W. Guo, T. Zhang, J. Song, T. Gao, Z. Gu, Y. Nie, Epitaxial growth and electronic structure of Ruddlesden–Popper nickelates ($La_{n+1}Ni_nO_{3n+1}$, n = 1–5). *APL Mater.* **8**, 091112 (2020).
25. J. Lee, I. Tung, S.-H. Chang, A. Bhattacharya, D. Fong, J. Freeland, H. Hong, In situ surface/interface x-ray diffractometer for oxide molecular beam epitaxy. *Rev. Sci. Instrum.* **87**, 013901 (2016).
26. H. Sun, Z. Mao, T. Zhang, L. Han, T. Zhang, X. Cai, X. Guo, Y. Li, Y. Zang, W. Guo, J. Song, D. Ji, C. Gu, C. Tang, Z. Gu, N. Wang, Y. Zhu, D. Schlom, Y. Nie, X. Pan, Chemically specific termination control of oxide interfaces via layer-by-layer mean inner potential engineering. *Nat. Commun.* **9**, 2965 (2018).
27. M. Sullivan, M. Ward, A. Gutiérrez-Llorente, E. R. Adler, H. Joress, A. Woll, J. Brock, Complex oxide growth using simultaneous in situ reflection high-energy electron diffraction and x-ray reflectivity: When is one layer complete? *Appl. Phys. Lett.* **106**, 031604 (2015).
28. X. Yan, F. Wrobel, Y. Li, H. Zhou, H.-h. Wang, A. Bhattacharya, J. Sun, H. Hong, D. D. Fong, In situ x-ray and electron scattering studies of oxide molecular beam epitaxial growth. *APL Mater.* **8**, 101107 (2020).
29. Y. Nie, Y. Zhu, C.-H. Lee, L. F. Kourkoutis, J. A. Mundy, J. Junquera, P. Ghosez, D. Baek, S. Sung, X. X. Xi, K. Shen, D. Muller, D. Schlom, Atomically precise interfaces from non-stoichiometric deposition. *Nat. Commun.* **5**, 4530 (2014).
30. W. Wei, K. Shin, H. Hong, Y. Shin, A. S. Thind, Y. Yang, R. F. Klie, F. J. Walker, C. H. Ahn, Solid state reduction of nickelate thin films. *Phys. Rev. Mater.* **7**, 013802 (2023).
31. J. Haeni, C. Theis, D. Schlom, W. Tian, X. Pan, H. Chang, I. Takeuchi, X.-D. Xiang, Epitaxial growth of the first five members of the $Sr_{n+1}Ti_nO_{3n+1}$ Ruddlesden–Popper homologous series. *Appl. Phys. Lett.* **78**, 3292–3294 (2001).
32. Y. Yacoby, M. Sowwan, E. Stern, J. O. Cross, D. Brewe, R. Pindak, J. Pitney, E. M. Dufresne, R. Clarke, Direct determination of epitaxial interface structure in Gd_2O_3 passivation of GaAs. *Nat. Mater.* **1**, 99–101 (2002).
33. D. Ferenc Segedin, B. H. Goodge, G. A. Pan, Q. Song, H. LaBollita, M.-C. Jung, H. El-Sherif, S. Doyle, A. Turkiewicz, N. K. Taylor, J. A. Mason, A. T. N'Diaye, H. Paik, I. E. Baggari, A. S. Botana, L. F. Kourkoutis, C. M. Brooks, J. A. Mundy, Limits to the strain engineering of layered square-planar nickelate thin films. *Nat. Commun.* **14**, 1468 (2023).
34. M. Osada, K. Fujiwara, T. Nojima, A. Tsukazaki, Improvement of superconducting properties in $La_{1-x}Sr_xNiO_2$ thin films by tuning topochemical reduction temperature. *Phys. Rev. Mater.* **7**, L051801 (2023).
35. Z. Wang, G.-M. Zhang, Y.-f. Yang, F.-C. Zhang, Distinct pairing symmetries of superconductivity in infinite-layer nickelates. *Phys. Rev. B* **102**, 220501 (2020).
36. N. N. Wang, M. W. Yang, Z. Yang, K. Y. Chen, H. Zhang, Q. H. Zhang, Z. H. Zhu, Y. Uwatoko, L. Gu, X. L. Dong, J. P. Sun, K. Jin, J.-G. Cheng, Pressure-induced monotonic enhancement of T_c to over 30 K in superconducting $Pr_{0.82}Sr_{0.18}NiO_2$ thin films. *Nat. Commun.* **13**, 4367 (2022).
37. G. Krieger, L. Martinelli, S. Zeng, L. Chow, K. Kummer, R. Arpaia, M. M. Sala, N. B. Brookes, A. Ariando, N. Viart, M. Salluzzo, G. Ghiringhelli, D. Preziosi, Charge and spin order dichotomy in $NdNiO_2$ driven by the capping layer. *Phys. Rev. Lett.* **129**, 027002 (2022).
38. F. Lechermann, Emergent flat-band physics in $d^{9-\delta}$ multilayer nickelates. *Phys. Rev. B* **105**, 155109 (2022).
39. S. Kunisada, S. Isono, Y. Kohama, S. Sakai, C. Bareille, S. Sakuragi, R. Noguchi, K. Kurokawa, K. Kuroda, Y. Ishida, S. Adachi, R. Sekine, T. K. Kim, C. Cacho, S. Shin, T. Tohyama, K. Tokiwa, T. Kondo, Observation of small Fermi pockets protected by clean CuO_2 sheets of a high-T_C superconductor. *Science* **369**, 833–838 (2020).
40. A. Ikeda, Y. Krockenberger, H. Irie, M. Naito, H. Yamamoto, Direct observation of infinite NiO_2 planes in $LaNiO_2$ films. *Appl. Phys. Express* **9**, 061101 (2016).
41. M. Osada, B. Y. Wang, K. Lee, D. Li, H. Y. Hwang, Phase diagram of infinite layer praseodymium nickelate $Pr_{1-x}Sr_xNiO_2$ thin films. *Phys. Rev. Mater.* **4**, 121801 (2020).
42. Y. Yu, L. Ma, P. Cai, R. Zhong, C. Ye, J. Shen, G. D. Gu, X. H. Chen, Y. Zhang, High-temperature superconductivity in monolayer $Bi_2Sr_2CaCu_2O_{8+\delta}$. *Nature* **575**, 156–163 (2019).
43. Q.-Y. Wang, Z. Li, W.-H. Zhang, Z.-C. Zhang, J.-S. Zhang, W. Li, H. Ding, Y.-B. Ou, P. Deng, K. Chang, J. Wen, C.-L. Song, K. He, J.-F. Jia, S.-H. Ji, Y.-Y. Wang, L.-L. Wang, X. Chen, X.-C. Ma, Q.-K. Xue, Interface-induced high-temperature superconductivity in single unit-cell FeSe films on $SrTiO_3$. *Chinese Phys. Lett.* **29**, 037402 (2012).
44. S. Tan, Y. Zhang, M. Xia, Z. Ye, F. Chen, X. Xie, R. Peng, D. Xu, Q. Fan, H. Xu, J. Jiang, T. Zhang, X. Lai, T. Xiang, J. Hu, B. Xie, D. Feng, Interface-induced superconductivity and strain-dependent spin density waves in FeSe/$SrTiO_3$ thin films. *Nat. Mater.* **12**, 634–640 (2013).
45. J. Lee, F. Schmitt, R. Moore, S. Johnston, Y.-T. Cui, W. Li, M. Yi, Z. Liu, M. Hashimoto, Y. Zhang, D. H. Lu, T. P. Devereaux, D.-H. Lee, Z.-X. Shen, Interfacial mode coupling as the origin of the enhancement of T_c in FeSe films on $SrTiO_3$. *Nature* **515**, 245–248 (2014).
46. B. H. Goodge, B. Geisler, K. Lee, M. Osada, B. Y. Wang, D. Li, H. Y. Hwang, R. Pentcheva, L. F. Kourkoutis, Resolving the polar interface of infinite-layer nickelate thin films. *Nat. Mater.* **22**, 466–473 (2023).

47. B.-X. Wang, H. Zheng, E. Krivyakina, O. Chmaissem, P. P. Lopes, J. W. Lynn, L. C. Gallington, Y. Ren, S. Rosenkranz, J. Mitchell, D. Phelan, Synthesis and characterization of bulk $Nd_{1-x}Sr_xNiO_2$ and $Nd_{1-x}Sr_xNiO_3$. *Phys. Rev. Mater.* **4**, 084409 (2020).
48. P. Puphal, Y.-M. Wu, K. Fürsich, H. Lee, M. Pakdaman, J. A. Bruin, J. Nuss, Y. E. Suyolcu, P. A. van Aken, B. Keimer, M. Isobe, M. Hepting, Topotactic transformation of single crystals: From perovskite to infinite-layer nickelates. *Sci. Adv.* **7**, eabl8091 (2021).
49. H. Sun, M. Huo, X. Hu, J. Li, Z. Liu, Y. Han, L. Tang, Z. Mao, P. Yang, B. Wang, J. Cheng, D.-X. Yao, G.-M. Zhang, M. Wang, Signatures of superconductivity near 80 K in a nickelate under high pressure. *Nature* **621**, 493–498 (2023).
50. H. S. Kum, H. Lee, S. Kim, S. Lindemann, W. Kong, K. Qiao, P. Chen, J. Irwin, J. H. Lee, S. Xie, S. Subramanian, J. Shim, S.-H. Bae, C. Choi, L. Ranno, S. Seo, S. Lee, J. Bauer, H. Li, K. Lee, J. A. Robinson, C. A. Ross, D. G. Schlom, M. S. Rzchowski, C.-B. Eom, J. Kim, Heterogeneous integration of single-crystalline complex-oxide membranes. *Nature* **578**, 75–81 (2020).
51. G.-M. Zhang, Y.-f. Yang, F.-C. Zhang, Self-doped Mott insulator for parent compounds of nickelate superconductors. *Phys. Rev. B* **101**, 020501 (2020).
52. K. Lee, B. Y. Wang, M. Osada, B. H. Goodge, T. C. Wang, Y. Lee, S. Harvey, W. J. Kim, Y. Yu, C. Murthy, S. Raghu, L. F. Kourkoutis, H. Y. Hwang, Linear-in-temperature resistivity for optimally superconducting (Nd,Sr)NiO_2. *Nature* **619**, 288–292 (2023).

Acknowledgments: We thank J. F. Mitchell for insightful discussions. This research used resources of the Advanced Photon Source and Center for Nanoscale Materials, US Department of Energy (DOE) Office of Science user facilities operated for the DOE Office of Science by Argonne National Laboratory under contract number DE-AC02-06CH11357. **Funding:** This work was supported by the US Department of Energy, Office of Science, Basic Energy Sciences, Materials Sciences and Engineering Division. **Author contributions:** Conceptualization: X.Y., H. Zhou, and D.D.F. Methodology: X.Y., H.H., A.B., H. Zhou, and D.D.F. Data curation: X.Y., Hong Zheng, Y. Li, H.C., D.P.P., Hao Zheng, Z.Z., H.H., G.W., Y. Liu, and H. Zhou. Formal analysis: X.Y., Y. Li, H.C., G.W., Y. Liu, and H. Zhou. Funding acquisition: A.B. and D.D.F. Writing—original draft: X.Y., H. Zhou, and D.D.F. Writing—review and editing: all authors. **Competing interests:** The authors declare that they have no competing interests. **Data and materials availability:** All data needed to evaluate the conclusions in the paper are present in the paper and/or the Supplementary Materials.

Submitted 2 February 2024
Accepted 26 November 2024
Published 1 January 2025
10.1126/sciadv.ado4572